

The Effect of Tissue Inhomogeneities on the Accuracy of Proton Path Reconstruction for Proton Computed Tomography

Kent Wong¹, Bela Erdelyi¹, Reinhard Schulte², Vladimir Bashkirov², George Coutrakon², Hartmut Sadrozinski³, Scott Penfold⁴, Anatoly Rosenfeld⁴

¹ *Department of Physics, Northern Illinois University, DeKalb, IL 60115*

² *Department of Radiation Medicine, Loma Linda University Medical Center, Loma Linda, CA 92354*

³ *Santa Cruz Institute of Particle Physics, University of California Santa Cruz, Santa Cruz, CA 95064*

⁴ *Centre for Medical Radiation Physics, University of Wollongong, Wollongong, NSW 2522, Australia*

Abstract. Maintaining a high degree of spatial resolution in proton computed tomography (pCT) is a challenge due to the statistical nature of the proton path through the object. Recent work has focused on the formulation of the most likely path (MLP) of protons through a homogeneous water object and the accuracy of this approach has been tested experimentally with a homogeneous PMMA phantom. Inhomogeneities inside the phantom, consisting of, for example, air and bone will lead to unavoidable inaccuracies of this approach. The purpose of this ongoing work is to characterize systematic errors that are introduced by regions of bone and air density and how this affects the accuracy of proton CT in surrounding voxels both in terms of spatial and density reconstruction accuracy. Phantoms containing tissue-equivalent inhomogeneities have been designed and proton transport through them has been simulated with the GEANT 4.9.0 Monte Carlo tool kit. Various iterative reconstruction techniques, including the classical fully sequential algebraic reconstruction technique (ART) and block-iterative techniques, are currently being tested, and we will select the most accurate method for this study.

Keywords: proton computed tomography, proton path simulation, GEANT4 simulation

PACS: 87.59.Fm Computed tomography (CT); 87.57.Ce Image quality: contrast, resolution, noise, etc.; 87.57.Gg Image reconstruction and registration

INTRODUCTION

Proton computed tomography (pCT) has been increasingly studied as an alternative to x-ray CT (xCT) in terms of more accurately predicting the proton Bragg peak position in the patient and imaging the patient in the treatment room for image-guided and adaptive proton radiation therapy (1). Relative electron density distributions can be directly measured with pCT; this makes pCT more suitable than conventional x-rays for the planning of proton radiation treatment. Presently, proton dose calculations are performed by xCT, and patients are positioned with the aid of x-ray radiographs, as megavoltage or orthovoltage cone-beam CT is not yet widely performed in existing proton treatment centers. The present uncertainties of xCT-based proton treatment planning are the results of the conversion of Hounsfield values to relative electron density values (2). The accuracy of proton treatment planning is also limited due to the difference

of physical interactions between photons and protons (3). In order to minimize these uncertainties, the long-term goal for developing the capability of pCT instead of xCT becomes important (4).

The modern approach to pCT requires tracking the individual protons traversing through an object from many projection directions and measuring their energy loss on the exit side (1). The mean energy loss of a proton can be related to the integrated electron density along the proton's path L with the equation

$$\int_{E_{in}}^{E_{out}} \frac{dE}{S(E, I_{water})} = \int_L \eta_e(r) dL \quad (1)$$

where S is the proton stopping power as a function of proton energy E , the mean excitation potential of the medium is assumed to be that of water, I_{water} , and η_e is the relative electron density. The entirety of the electron density information can then be used to

reconstruct the object's electron density in 3D (5) for example, with the algebraic reconstruction technique (ART) (6).

Limiting physical factors of pCT included energy-loss straggling and multiple Coulomb scattering (MCS), which affect the electron density resolution and spatial resolution respectively. Energy straggling is attributed to the protons' inelastic collisions with the material's outer atomic electrons when the protons are traversing that material; these collisions lead to random energy loss due to ionizations and excitations. In contrast, MCS is the result of elastic interaction between the material's nuclei and protons, causing negligible energy loss but multiple small-angle scattering (i.e., lateral and angular displacement of the proton from its incident direction). These two factors primarily contribute to the quality of the pCT image. Additionally, protons may undergo non-elastic nuclear interactions, which attenuate proton fluence with increasing depth but do not influence image quality if these events are excluded by appropriate data cuts (5).

To improve the spatial resolution of proton radiography and proton CT, *most likely path* (MLP) formalisms have been developed (7-9). These algorithms assume that complete or partial entry and exit information consisting of spatial and angular data in the object reference system. Modern pCT designs use silicon strip detectors (SSD) to measure the position and direction of individual protons prior to and post traversing the object (1). Initially, Schneider and Pedroni (7) derived a formula for the spatial resolution of transmission proton radiography with the measured points and angles of proton trajectory. Williams (8) introduced a χ^2 estimator and solved the expressions for lateral displacement and direction that will minimize χ^2 by setting its derivative to zero. The resulting lateral and angular deviation from known entry parameters gives the most likely trajectory of the proton. Schulte et al. (9) developed a more compact and flexible version of William's formalism. These MLP formalisms are mathematically equivalent and are based on the same assumptions; namely, they all assume uniform water density throughout the reconstruction volume.

This paper compares the analytical MLPs using the formalism presented in (9) with the actual paths of GEANT4-simulated protons traversing an inhomogeneous phantom consisting of slabs of air, bone and water (Fig. 1). The goal of this study was to qualitatively and quantitatively describe the presence of typical inhomogeneities of the human body on the accuracy of the MLP description in order to test the adequacy of the assumption of homogeneous water and to guide the development of more sophisticated MLP algorithms.

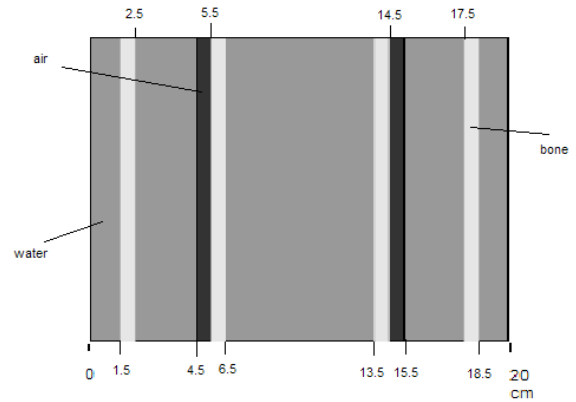


FIGURE 1. Inhomogeneous phantom with four 1-cm bone slabs (lightly shaded), two 1-cm air slabs (darkly shaded), and five intervening water slabs (intermediately shaded).

Assuming the knowledge of the entry and exit lateral displacements and the exit direction, we can estimate the lateral displacement and direction at any depth in the phantom. Thus, we can eventually plot out the maximum likelihood proton path with these displacements. GEANT4 was used to generate a random set of lateral t values and direction for each of simulated 19,995 protons through the inhomogeneous phantom. Statistical analyses were conducted to describe the accuracy of the analytical MLPs based on the assumption of a homogeneous object.

METHODS

Maximum Likelihood Proton Path Formalism

Fig. 2 shows, as an example, the GEANT4-simulated and calculated path for two protons.

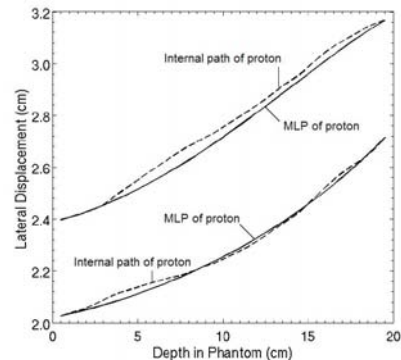


FIGURE 2. The MLPs and GEANT4 internal paths for two simulated protons. The MLP error at each depth is defined as the difference between the lateral displacement of the simulated path and the MLP of a proton traversing the inhomogeneous phantom of 20 cm maximum depth (Fig. 1).

The matrix-based two-dimensional (2D) MLP, assuming a homogeneous phantom of water density, was calculated according to (9) from the known entry and exit displacements and exit direction:

$$y_{MLP} = (\Sigma_1^{-1} + R_1^T \Sigma_2^{-1} R_1)^{-1} (\Sigma_1^{-1} R_0 y_0 + R_1^T \Sigma_2^{-1} y_2) \quad (2)$$

where

$$\Sigma_1 = \begin{pmatrix} \sigma_{t_1}^2 & \sigma_{t_1\theta_1}^2 \\ \sigma_{t_1\theta_1}^2 & \sigma_{\theta_1}^2 \end{pmatrix} \quad (3),$$

$$\Sigma_2 = \begin{pmatrix} \sigma_{t_2}^2 & \sigma_{t_2\theta_2}^2 \\ \sigma_{t_2\theta_2}^2 & \sigma_{\theta_2}^2 \end{pmatrix} \quad (4),$$

$$R_0 = \begin{pmatrix} 1 & u_1 - u_0 \\ 0 & 1 \end{pmatrix} \quad (5),$$

$$R_1 = \begin{pmatrix} 1 & u_2 - u_1 \\ 0 & 1 \end{pmatrix} \quad (6),$$

$$y_0 = \begin{pmatrix} t_0 \\ \theta_0 \end{pmatrix} \quad (7),$$

and

$$y_2 = \begin{pmatrix} t_2 \\ \theta_2 \end{pmatrix} \quad (8).$$

The vector y_{MLP} is the trajectory

$$y_1 = \begin{pmatrix} t_1 \\ \theta_1 \end{pmatrix} \quad (9)$$

that maximizes the posterior likelihood of finding the proton with the lateral displacement t_1 and direction at an intermediate depth of u_1 in the material given known entry parameters y_0 at entry depth u_0 (set as 0 cm) and y_2 at the exit depth u_2 (set as 20 cm) (Fig. 3) (9). The matrices Σ_1 and Σ_2 are the variance-covariance scattering matrices defined at any depth from 0 to u_1 and from u_1 to 20 cm, respectively. These scattering matrices contain elements of variances and covariances of t and θ (8):

$$\sigma_{t_1}^2(u_1) = \Theta_0^2 \int_0^{u_1} \frac{(u_1 - u)^2}{\beta^2(u)p^2(u)} \frac{du}{X_0} \quad (10),$$

$$\sigma_{\theta_1}^2(u_1) = \Theta_0^2 \int_0^{u_1} \frac{1}{\beta^2(u)p^2(u)} \frac{du}{X_0} \quad (11),$$

$$\sigma_{t_1\theta_1}^2(u_1) = \Theta_0^2 \int_0^{u_1} \frac{u_1 - u}{\beta^2(u)p^2(u)} \frac{du}{X_0} \quad (12),$$

$$\sigma_{t_2}^2(u_1, u_2) = \Theta_0^2 \int_{u_1}^{u_2} \frac{(u_2 - u)^2}{\beta^2(u)p^2(u)} \frac{du}{X_0} \quad (13),$$

$$\sigma_{\theta_2}^2(u_1, u_2) = \Theta_0^2 \int_{u_1}^{u_2} \frac{1}{\beta^2(u)p^2(u)} \frac{du}{X_0} \quad (14),$$

$$\sigma_{t_2\theta_2}^2(u_1, u_2) = \Theta_0^2 \int_{u_1}^{u_2} \frac{u_2 - u_1}{\beta^2(u)p^2(u)} \frac{du}{X_0} \quad (15).$$

The constant in front of all integrals is $\Theta_0 = 13.6$ MeV/c and the radiation length for water is $X_0 = 36.1$ cm. Further, β is the proton's velocity relative to the speed of light, and p is its momentum. The first row, first column element of the error matrix

$$\varepsilon_{t_1\theta_1}(u_1) = 2(\Sigma_1^{-1} + R_1^T \Sigma_2^{-1} R_1)^{-1} \quad (16)$$

gives the uncertainty in the lateral displacement at depth u_1 .

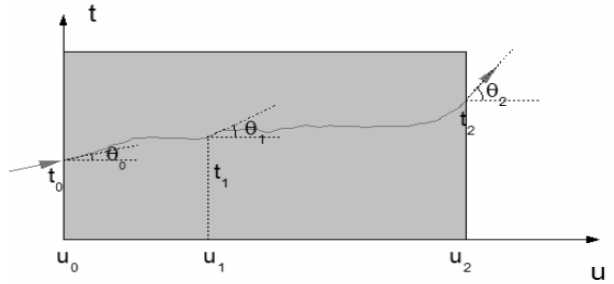


FIGURE 3. Geometry of the path of a proton through an object in the t - u -plane (reproduced from (9)). The t - u coordinate system is determined by the external silicon tracking detectors. A proton enters from the left with known lateral displacement and direction and exits the object after traversing a depth $(u_2 - u_0)$ with known exit location and angle. The lateral displacement and direction at an intermediate depth u_1 are unknown but its most likely values can be calculated using Bayes' law. The entirety of locations and directions inside the object yields the MLP in the t - u -plane.

GEANT4 Simulation and Data Analysis

As suggested in (8) and (9), a fifth-degree polynomial was fitted to the term $1/\beta^2(u)p^2(u)$, such that

$$\frac{1}{\beta^2(u)p^2(u)} = a_0 + a_1u + a_2u^2 + a_3u^3 + a_4u^4 + a_5u^5 \quad (17),$$

in order to avoid numerical integration of the scattering elements. The resulting parameters based on a GEANT4 simulation with a 200 MeV monoenergetic

proton pencil beam traversing a 20-cm thick water absorber in ascending subscript order are $7.457 \times 10^{-6} \text{ c}^2/\text{MeV}^2$, $4.548 \times 10^{-7} \text{ c}^2/\text{MeV}^2\text{cm}^{-1}$, $-5.777 \times 10^{-8} \text{ c}^2/\text{MeV}^2\text{cm}^{-2}$, $1.301 \times 10^{-8} \text{ c}^2/\text{MeV}^2\text{cm}^{-3}$, $-9.228 \times 10^{-10} \text{ c}^2/\text{MeV}^2\text{cm}^{-4}$, $2.687 \times 10^{-11} \text{ c}^2/\text{MeV}^2\text{cm}^{-5}$ (9).

The GEANT4 simulation employed a uniform fan beam of 200 MeV protons incident on a water cube (Fig. 4). Simulations were performed for the phantom shown in Fig. 1 and a homogeneous but otherwise equivalent water phantom for comparison. The initial proton fan beam spread was approximately $\pm 2.86^\circ$ resulting in a width of 16 cm at the 20 cm entry plane of the phantom. The source was located 160 cm away from the entry plane of the water cube. At the entry plane ($u_0 = 0$) the maximum beam spread was $\pm 3.27^\circ$, whereas at the exit plane of the cube protons spanned the entire 20 cm width with exit directions ranging from $\pm 11.5^\circ$. Statistical analysis was conducted on 1600 protons randomly chosen out of the 19,995 histories generated from GEANT4. A total of 127 histories were excluded from the sample because their exit energy and/or angle was outside a 3-sigma interval of the energy and angle of the protons from the same spatial bin.

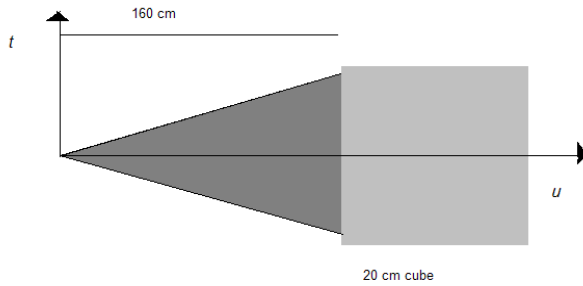


FIGURE 4. A proton source 160 cm away from the entry plane of a 20-cm water cube has a spread of $\pm 2.86^\circ$.

For each of the 1,600 protons, the 2D MLP was calculated using the formalism and polynomial coefficients described above. These were subtracted from the Monte-Carlo-simulated 3D proton tracks projected onto the t - u plane to obtain the individual MLP error as a function of depth. Finally, summary statistics, mean and root mean square (rms) error, as well as the 95% confidence limits of the mean, were calculated as a function of depth in the phantom.

RESULTS

Fig. 5 shows mean and rms MLP errors as a function of depth based on the analysis of the random sample of 1,600 simulated proton tracks and their MLPs. The figure plots out the longitudinal profile of the 20-cm phantom. The rms MLP error for the

homogenous water phantom is shown for comparison. Note that, despite the discontinuities in electron density (water, air, and bone) the mean MLP error showed no systematic discontinuities. The maximum mean MLP error was 0.03 mm and at no depth, the mean error was significantly different from zero as indicated by the 95% confidence interval always including the value zero. For both phantoms, the standard deviation peaked at 0.6 mm at a depth of 12 cm, i.e., slightly beyond the center of the phantom. The maximum rms MLP error at this point was about 20% higher for the inhomogeneous phantom than for the homogeneous phantom.

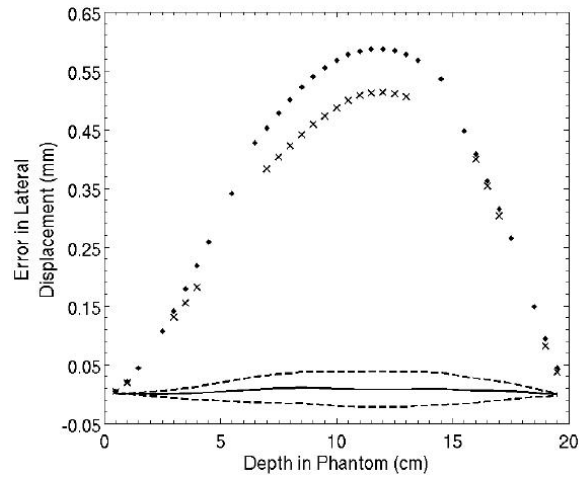


FIGURE 5. Mean of the MLP error shown as the lower solid line. The 95% confidence limits of the mean are displayed as the upper and lower dashed lines surrounding the mean. The upper points correspond to the rms MLP error of the inhomogeneous phantom and the lower points to the rms error of the homogeneous phantom.

DISCUSSION AND CONCLUSIONS

As suggested by Williams (8), an important characteristic of MCS, which allows an analytical formulation for the MLP using the χ^2 formalism, is the Gaussian distribution of the scattering angle and lateral displacement when large-angle scattering events are excluded. William's MLP formalism is based on the assumption of a homogeneous object. Our work shows that on average the derived MLPs show a relatively good fit to the GEANT4 simulated proton paths despite the bone slabs and air cavities included in the phantom. The mean MLP error was not significantly different from zero (Fig. 5), which indicates that the inhomogeneities did not introduce a significant systematic error in the MLP. Thus, most proton paths will more or less trace out the MLP if large angular events are not taken into account. Similar to the result

found in a homogeneous water phantom (9), the standard deviation of the MLP error is of the order of 0.6 mm in the inhomogeneous 20-cm phantom and about 20% larger than in the homogenous phantom. This result is not unexpected because the bone inhomogeneity will introduce additional scattering not taken into account in the MLP calculation that assumes homogenous water composition.

We have not yet examined the influence of inhomogeneities with finite lateral dimension on the accuracy of the MLP under the assumption of a homogeneous water composition. Due to the discontinuity in the scattering of protons at a lateral boundary of an inhomogeneity it is conceivable that a systematic MLP error will be introduced locally.

REFERENCES

1. R. Schulte, V. Bashkirov, T. Li, J.Z. Liang, K Mueller, J. Heimann, L. Johnson, B. Keeney, H. F-W Sadrozinski, A. Seiden, D.C. Williams, L. Zhang, Z. Li, S. Peggs, T. Satogata, and C. Woody, *IEEE Trans. Nucl. Sci.* **51**, 866-872 (2004).
2. U. Schneider, E. Pedroni, and A. Lomax, *Phys. Med. Biol.* **41**, 111-124 (1996).
3. U. Schneider and E. Pedroni, *Med. Phys.*, **22**, 353-363 (1995).
4. H. F.-W. Sadrozinski, V. Bashkirov, M. Bruzzi, L. R. Johnson, B. Keeney, G. Ross, R. W. Schulte, A. Seiden, K. Shahnazi, D. C. Williams, and L. Zhang. *Nucl. Instrum. Methods Phys. Res. A* **511**, 275-281 (2003).
5. R.W. Schulte, V. Bashkirov, M.C. Loss Klock, T. Li, A.J. Wroe, I. Evseev, D.C. Williams, and T. Satogata, *Med. Phys.* **32**, 1035-1046 (2005).
6. T. Li, Z. Liang, J. V. Singanallur, T. J. Satogata, D. C. Williams, and R. W. Schulte, *Med. Phys.* **33**, 699-706 (2006).
7. U. Schneider and E. Pedroni, *Med. Phys.* **21**, 1657-1663 (1994).
8. D. C. Williams, *Phys. Med. Biol.* **49**, 2899-2911 (2004).
9. R.W. Schulte, S.N. Penfold, J.T. Tafas, K.E. Schubert, *Med. Phys.* **35**, 4849- 4856 (2008).